

# Quasiparticle model of quark-gluon plasma at imaginary chemical potential

M. Bluhm<sup>1</sup> and B. Kämpfer<sup>1,2</sup><sup>1</sup>*Forschungszentrum Dresden-Rossendorf, PF 510119, 01314 Dresden, Germany*<sup>2</sup>*Institut für Theoretische Physik, TU Dresden, 01062 Dresden, Germany*

(Received 6 November 2007; published 4 February 2008)

A quasiparticle model of the quark-gluon plasma is compared with lattice QCD data for purely imaginary chemical potential. Net quark number density, susceptibility as well as the deconfinement border line in the phase diagram of strongly interacting matter are investigated. In addition, the impact of baryochemical potential dependent quasiparticle masses is discussed. This accomplishes a direct test of the model for nonzero baryon density. The found results are compared with lattice QCD data for real chemical potential by means of analytic continuation and with a different (independent) set of lattice QCD data at zero chemical potential.

DOI: [10.1103/PhysRevD.77.034004](https://doi.org/10.1103/PhysRevD.77.034004)

PACS numbers: 12.38.Mh, 12.39.-x

## I. INTRODUCTION

Strongly interacting matter, as described by QCD, exhibits an astonishingly rich phase structure. In the region of not too large baryon densities, the deconfinement transition from hadronic matter to a plasma built of quark-gluon constituents is the most prominent feature. It is signaled by a rapid change in the expectation value of the Polyakov loop and the chiral condensate where one assigns a pseudocritical temperature  $T_c$  to this transition (cf. reviews, e.g. [1]). At higher temperatures,  $T > 3T_c$ , further structural changes are conjectured [2]. For nonzero quark chemical potential  $\mu$ , corresponding to a finite net baryon density, many researchers argue on the change of the deconfinement border line, representing an analytic crossover, into a first-order transition curve. The onset of this sequence of first-order transitions is marked by a critical point being of second order which has attracted much attention recently (see [3]). The interest in this part of the phase diagram is triggered by the possibility to probe it under laboratory conditions in relativistic heavy-ion collisions.

With the advance of precision data from ultrarelativistic heavy-ion collisions at RHIC, the paradigm on the quark-gluon plasma has changed [4]: The notion of a strongly coupled plasma has been put forward to explain the seemingly very small viscosity to entropy ratio deduced from hydrodynamical fits to experimental data as in [5], and various models have been developed [6] to account for such a property. On the other hand, we are witnessing a vast progress in first-principle calculations of thermodynamic properties of hot strongly interacting matter based directly on QCD [7–9]. While various observables such as pressure, energy density or numerous susceptibilities are addressed, the available lattice QCD data are obtained for different numerical setups, lattice sizes, flavor numbers and quark masses as well. Particular attempts are needed to access nonzero baryon densities because the notorious sign problem of the fermion determinant prevents a direct application of methods useful for zero baryon density. Nevertheless, a few methods have been developed to ac-

cess nonzero baryon densities. Among such methods is the calculation of thermodynamic quantities at purely imaginary chemical potential. Here, the sign problem is avoided but the results have to be analytically continued to real chemical potential. In this respect it is useful to have a model at our disposal which is successfully probed for both real and imaginary chemical potential in order to accomplish the translation of results from imaginary to real chemical potential.

While baryon density effects are small for heavy-ion collisions at top-RHIC energies and will be even smaller for LHC energies, at least in the midrapidity region, they are sizeable for CERN-SPS and upcoming FAIR energies. In this respect, a firm knowledge of thermodynamic bulk properties of strongly interacting matter is highly desirable. As a step towards achieving this goal we are going to extend our quasiparticle model [10–13] to imaginary chemical potential. Here, information is obtained for  $\mu^2 < 0$  allowing, in principle, for identifying  $\mu = \pm i\mu_i$ . The model has been tested successfully for real chemical potential [14], say in describing the Taylor expansion coefficients of the pressure as a series in powers of  $\mu/T$ . In such a way, Peshier's flow equation [11] is tested in some detail. This flow equation transports information about the effective coupling,  $G^2$ , from the temperature axis to nonzero  $\mu$  and determines to a large extent the dependence on  $\mu$  and thus on baryon density. Another important piece of the model is the quasiparticle ansatz for dynamically generated effective masses of quarks  $\propto (T^2 + \frac{\mu^2}{\pi^2})G^2$ . When going to purely imaginary chemical potential  $\mu \rightarrow \pm i\mu$  the sign of the  $\mu^2$  term is flipped, as also signs in Peshier's flow equation are changed. Therefore, the  $\mu$  dependence of the model is directly tested by considering an imaginary chemical potential.

In the following, two symmetries of the QCD partition function  $Z(T, \mu)$  are of relevance: (i)  $Z(T, \mu) = Z(T, -\mu)$ , and (ii)  $Z(T, i\mu_i) = Z(T, i(\mu_i + \frac{2\pi}{3}T))$ , i.e.  $Z(T, \mu)$  is periodic in  $\mu_i$  with period  $2\pi T/3$  [15]. Symmetry (i) makes  $Z$  an even function of  $\mu$  (meaning that in a Taylor series

expansion only even powers of  $\mu/T$ , and thus also of  $\mu_i/T$ , are encountered) such that we can focus on  $\mu = +i\mu_i$  only, while (ii) implies the Roberge-Weiss periodicity [15] which is anchored in the center symmetry. This periodicity is characterized by lines of first-order transitions ( $Z_3$  transitions) at  $\mu_i = \frac{\pi}{3}T(1 + 2k)$  for all integers  $k$  and sufficiently high temperature  $T$  while for smaller temperatures the behavior of thermodynamic quantities is analytic. The endpoint of first-order transitions,  $T^E$ , is determined by the crossing of the Roberge-Weiss transition line with the chiral critical line which is also a first-order transition line for  $N_f = 4$  degenerate quark flavors [16]. The Roberge-Weiss periodicity implies that in the  $T - \mu_i/T$  plane all sectors between  $\mu_i/T = \frac{2\pi}{3}k$  and  $\mu_i/T = \frac{2\pi}{3}(k + 1)$  are copies of the sector between  $\mu_i/T = 0$  and  $\mu_i/T = \frac{2\pi}{3}$ . Furthermore, the subsector between  $\mu_i/T = \pi/3$  and  $\mu_i/T = 2\pi/3$  is an reflected copy of the subsector between  $\mu_i/T = 0$  and  $\mu_i/T = \pi/3$  mirrored at the first Roberge-Weiss transition line. As thermodynamic quantities behave nonanalytically at  $\mu_i/T = \pi/3$  (Roberge-Weiss transition), an analytic continuation of results obtained for imaginary chemical potential to real  $\mu$  has direct access to the region  $\mu < \pi/3T$  only.

Because of the severe approximations made when linking our phenomenological model [10,11,13] to QCD as presented in [12], the Roberge-Weiss periodicity is not longer apparent. Having this in mind, we translate the model to imaginary chemical potential in Sec. II. The comparison with lattice QCD data at imaginary chemical potential is performed in Sec. III, where also the continuation to real chemical potential is presented. This allows, in addition, for a comparison with another and independent set of lattice QCD data obtained at  $\mu = 0$  (Sec. IV). Furthermore, we investigate in detail the impact of the baryochemical potential dependence of the quasiquark and quasigluon masses (self-energies) on the found results and discuss the deconfinement border line in the phase diagram of strongly interacting matter. Our results are summarized in Sec. V. Appendices A and B contain Peshier's flow equation for imaginary chemical potential and a discussion about the parametrization of the  $\mu$  dependence of the density.

## II. QUASIPARTICLE MODEL AT IMAGINARY CHEMICAL POTENTIAL

The employed model is constructed by assuming a quasiparticle picture for the QCD pressure or quark number density (the explicit expression for the pressure is relegated to Appendix A) using dynamically generated effective masses for the quasiquarks and quasigluons. The entering QCD running coupling is replaced by an effective coupling  $G^2(T, \mu)$  which is subject to Peshier's flow equation [11] resting on a thermodynamic self-consistency condition and the stationarity of the grand canonical potential  $\Omega = -pV = -T \ln Z$ , where  $p$  de-

notes the pressure and  $V$  the volume of the system. Straightforward replacement of  $\mu = i\mu_i$  in  $p(T, \mu)$  renders the net quark number density,  $n(T, i\mu_i) = -i\partial p(T, i\mu_i)/\partial \mu_i$ , related to the net baryon density  $n_B = \frac{1}{3}n$ , to

$$n(T, i\mu_i) = \frac{d_q}{2\pi^2} \int_0^\infty dk k^2 \left( \frac{1}{e^{(\omega_q - i\mu_i)/T} + 1} - \frac{1}{e^{(\omega_q + i\mu_i)/T} + 1} \right) \quad (1)$$

$$= i \frac{d_q}{\pi^2} \int_0^\infty dk k^2 \left( \frac{e^{\omega_q/T} \sin(\mu_i/T)}{e^{2\omega_q/T} + 2e^{\omega_q/T} \cos(\mu_i/T) + 1} \right), \quad (2)$$

where  $d_q = 2N_c N_f$  is the degeneracy factor of quarks for  $N_c = 3$  colors and  $N_f$  quark flavors. The found result for  $n$  is purely imaginary and positive (negative) for small positive (negative)  $\mu_i$ , i.e.  $n$  is an odd function in  $\mu_i$ . Furthermore, for small  $\mu_i/T$ , i.e. for small  $\mu_i$  or large  $T$ , the  $\mu_i$  dependence of the net quark number density is to a good approximation linear in  $\mu_i$ .

The quark dispersion relation  $\omega_q(k)$  employed in Eqs. (1) and (2) reads

$$\omega_q^2 = k^2 + M_\infty^2 \quad (3)$$

with asymptotic mass  $M_\infty^2 = m_q^2 + 2M_+^2$  using

$$M_+^2 = \frac{N_c^2 - 1}{16N_c} \left( T^2 - \frac{\mu_i^2}{\pi^2} \right) G^2(T, i\mu_i) \quad (4)$$

as plasma frequency. This dispersion relation is based on a calculation of one-loop self-energies with finite quark masses  $m_q$  in Feynman gauge in the asymptotic limit [17] for small  $m_q/T$ , where  $m_q$  may be temperature dependent as well in order to allow for a direct comparison with lattice QCD data. In the following, we will fix the quark mass parameter  $m_q = 0.2T$  in line with the lattice QCD simulations considered in Secs. III and IV. (A different approximation of  $M_\infty$  is discussed in Sec. III C.) Equations (1) and (2) highlight the quasiparticle character of the model: the baryon charge is carried by excitations with dispersion relation given by Eq. (3). The dependence of  $M_\infty$  on the chemical potential (cf. [18]) will be discussed in Sec. III D.

Peshier's flow equation [11] for imaginary chemical potential reads

$$b = a_T \frac{\partial G^2}{\partial T} + a_{\mu_i} \frac{\partial G^2}{\partial \mu_i}, \quad (5)$$

where the coefficients  $b$ ,  $a_T$  and  $a_{\mu_i}$  depending on  $T$ ,  $\mu_i$  and  $G^2(T, i\mu_i)$  are relegated to Appendix A. Transforming Eq. (5) to a system of three coupled ordinary differential equations, it can be solved by the methods of characteristics knowing, for instance,  $G^2(T, \mu = 0)$ . A convenient parametrization of  $G^2(T, \mu = 0)$  is [11]

$$G^2(T \geq T_c, \mu = 0) = \frac{16\pi^2}{\beta_0 \log \xi^2}, \quad (6)$$

making some contact to perturbative QCD at very large temperatures, while in this paper we focus on the region  $T \geq T_c$ . Here,  $\beta_0 = \frac{1}{3}(11N_c - 2N_f)$  and  $\xi$  is parametrized phenomenologically as  $\xi = \lambda(T - T_s)/T_c$ , where the model parameters are a scale parameter  $\lambda$  necessary for the correct description of thermodynamics at large temperatures and a phenomenological infrared regulator  $T_s$

$$\begin{aligned} \chi(T, i\mu_i) = & \frac{d_q}{2\pi^2 T} \int_0^\infty dk k^2 \frac{(2e^{3\omega_q/T} \cos(\mu_i/T) + 4e^{2\omega_q/T} + 2e^{\omega_q/T} \cos(\mu_i/T))}{(e^{2\omega_q/T} + 2e^{\omega_q/T} \cos(\mu_i/T) + 1)^2} + \frac{d_q}{2\pi^2 T} \int_0^\infty dk \frac{k^2}{\omega_q} \\ & \times \frac{(e^{3\omega_q/T} \sin(\mu_i/T) - e^{\omega_q/T} \sin(\mu_i/T))}{(e^{2\omega_q/T} + 2e^{\omega_q/T} \cos(\mu_i/T) + 1)^2} \times \frac{N_c^2 - 1}{8N_c} \left( \frac{2}{\pi^2} \mu_i G^2 - \left[ T^2 - \frac{\mu_i^2}{\pi^2} \right] \frac{\partial G^2}{\partial \mu_i} \right); \end{aligned} \quad (7)$$

it is purely real and symmetric under  $\mu_i \rightarrow -\mu_i$  (cf. Appendix A). Furthermore, for small  $\mu_i$ , the first term in Eq. (7) is positive and dominates the second term. At  $\mu = 0$ , one finds

$$\chi(T, \mu = 0) = \frac{d_q}{\pi^2 T} \int_0^\infty dk k^2 \frac{e^{\tilde{\omega}_q/T}}{e^{2\tilde{\omega}_q/T} + 2e^{\tilde{\omega}_q/T} + 1} > 0, \quad (8)$$

where  $\tilde{\omega}_q = \omega_q(T, \mu = 0)$ .

### III. COMPARISON WITH LATTICE QCD RESULTS FOR IMAGINARY MU

#### A. Baryon density and quark number susceptibility

We confront now the above introduced quasiparticle model (QPM) with lattice QCD data [19,21] at nonzero  $T$  and  $\mu_i$  obtained for  $N_f = 4$  degenerate quark flavors with  $m_q = 0.2T$ ; these calculations [19,21] are performed on a lattice with temporal and spatial extensions  $N_\tau = 4$  and  $N_\sigma = 16$ . In some simulations with imaginary chemical potential  $\mu_i < 0$  is considered [22] implying a negative imaginary part of the net quark number density  $n(T, i\mu_i)$  according to Eq. (2). In the following, however, we will consider  $\mu_i > 0$  which renders the sign of  $n(T, i\mu_i)$  and accordingly the behavior of  $\chi = \partial n / \partial (i\mu_i)$ . Our model is formulated for a system infinite in space and time. Thus, we need a proper extrapolation of the lattice QCD data to the continuum limit ( $N_\tau \rightarrow \infty$  at fixed temperature). Different estimates for a continuum extrapolation are conceivable. For instance, one may select a scaling factor strictly valid only for asymptotically high temperatures, or one may use as scaling factor the ratio of thermodynamic quantities for a massless, noninteracting gas of quarks and gluons known in the continuum limit and from lattice QCD for finite  $N_\tau$ . Even though such estimates for a correction factor could depend on  $T$ , in general, we apply the latter procedure, assuming that the continuum

shifting the infrared divergence to  $T = T_s + T_c/\lambda < T_c$  for appropriate parameter values.

Results obtained for  $\mu^2 < 0$  need to be analytically continued into the  $\mu^2 > 0$  half-plane in order to achieve physical results. An effective analytic continuation requires a positive second derivative of  $Z$  with respect to  $\mu$ , cf. [19,20], i.e. the quark number susceptibility  $\chi(T, \mu) = \partial n(T, \mu) / \partial \mu > 0$ . The result for  $\chi$  reads for imaginary chemical potential

extrapolations for QCD and for the noninteracting gas of quarks and gluons are similar (cf. discussion in [23] for pure  $SU(3)$  theory). In principle, however, a profound extrapolation to the continuum limit should be based on simulations with different size lattices as leading corrections to the continuum limit are of the order  $\mathcal{O}(N_\tau^{-2})$  [1,23]. Taking the Stefan-Boltzmann result of  $n_B/T^3$  for  $N_\tau = 4$  [19], we find as educated guess for the needed continuum extrapolation factor of the net quark number density  $d_{\text{lat}}^{(n)} = 0.456$ . This compares well with continuum extrapolation factors reported in [24–26], reading 0.446 and 0.46, respectively, where similar actions have been used in the lattice simulations.

In Fig. 1, we compare our model with the continuum estimate of the lattice QCD data [19,21] for the scaled net quark number density as a function of  $\mu_i/T_c$  at constant  $T$ . Because  $n = 3n_B$  as a function of imaginary chemical potential is found to be purely imaginary, both in Eq. (2) and in the lattice calculations, we exhibit its imaginary part in the following. We adjust the QPM parameters of the effective coupling  $G^2(T, \mu = 0)$  in Eq. (6) in order to perfectly describe  $n/T^3$  at  $T = 1.1T_c$  reading  $T_s = 0.96T_c$  and  $\lambda = 56$  which shifts the divergence of  $G^2(T, \mu = 0)$  to approximately  $T = 0.98T_c$ . We utilize  $T_c = 163$  MeV as given in [16] for the case at hand. Note that we consider only temperatures  $T \geq T_c$ . The continuum extrapolated lattice QCD data, in particular, the pronounced bending of  $n/T^3$  for  $T = 1.1T_c$ , are impressively well described by the QPM parametrization. The drastic change in the slope for  $T = 1.1T_c$  signals the onset of the Roberge-Weiss transition at  $\mu_c/T_c = 11\pi/30$ , where  $n$  should exhibit a discontinuity. In the QPM, this change in slope is driven by the dependence of the quasiparticle asymptotic mass  $M_\infty$  on chemical potential and, in particular, by the behavior of  $G^2$  with respect to  $\mu_i$  as dictated by Peshier's flow equation Eq. (5). On the other hand, as evident from Eq. (2)  $n/T^3$  exhibits a

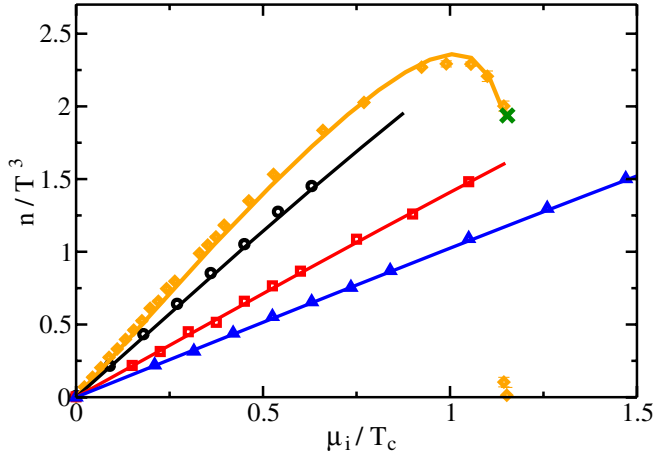


FIG. 1 (color online). Comparison of the QPM (solid curves) for the scaled net quark number density  $n/T^3$  as a function of  $\mu_i/T_c$  with continuum estimates of the lattice QCD data [19,21] for temperatures  $T = 1.1, 1.5, 2.5, 3.5 T_c$  (diamonds, circles, squares, and triangles, respectively). The fat cross depicts the Roberge-Weiss critical chemical potential  $\mu_c/T = \pi/3$  for  $T = 1.1T_c$ , where we stopped our calculations.

linear dependence on  $\mu_i$  for larger temperatures and small  $\mu_i$ . We note that  $n/T^3$  exhibited as a function of  $\mu_i/T$  shows almost no dependence on  $T$  for temperatures  $T \geq 1.5T_c$ . Below  $T_c$ , however,  $n/T^3$  displays a qualitatively different behavior being continuous and periodic as a function of  $\mu_i/T$  [19]. We choose the lattice QCD data at  $T = 1.1T_c$  for adjusting the QPM parameters as the pronounced bending close to  $\mu_c/T_c$  represents the most sensitive test of our model. In fact, the description of the linear behavior of  $n/T^3$  for all temperatures is rather robust under slight variations of the parameters, whereas the onset of the pronounced structure at  $T = 1.1T_c$  decisively depends on the parameter values. Therefore, a minimal  $\chi^2$ -fit to all available lattice QCD data is rather equivalent to a perfect fit to the data at  $1.1T_c$ .

Within the QPM, results obtained by considering purely imaginary chemical potential can easily be analytically continued to real  $\mu$ . This is achieved by continuing the purely imaginary variable  $\mu = i\mu_i$  to the entire complex plane and finally taking the limit  $\text{Im } \mu \rightarrow 0$ . In this way, we recover the quasiparticle model [10–12] formulated for real  $\mu$ . Within the analyticity domain, i.e. for  $\mu < \mu_c(T)$ , the analytic continuation is unique as guaranteed by general arguments. Keeping the QPM parameters  $\lambda$  and  $T_s$  fixed, the results of  $n/T^3$  for real  $\mu/T_c$  are exhibited in Fig. 2 (solid curves). These results may be compared to other analytic continuations. For instance, in [19], a polynomial fit to  $n/T^3$  as well as its analytic continuation to real  $\mu/T$  (dashed curves in Fig. 2) was considered. Despite the fact that this polynomial fit  $n(T, \mu_i, m_q) = a(T, m_q)\mu_i + b(T, m_q)\mu_i^3$  for imaginary chemical potential, with analytic continuation  $n(T, \mu, m_q) = a(T, m_q)\mu - b(T, m_q)\mu^3$ , cannot account for the change

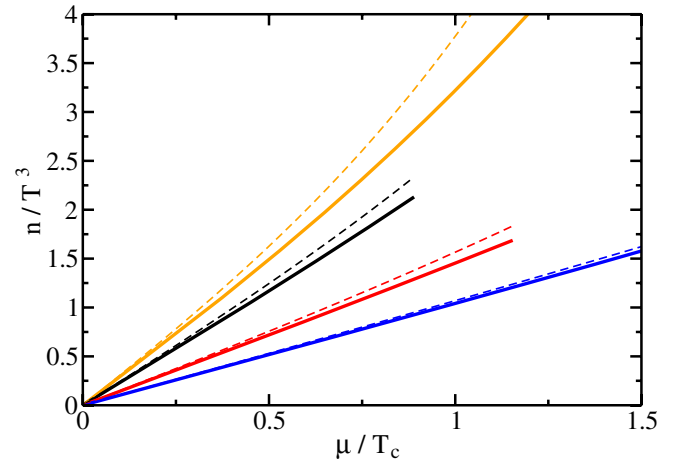


FIG. 2 (color online). Continuation of the QPM results for  $n/T^3$  exhibited in Fig. 1 to real chemical potential  $\mu/T_c$  (solid curves) for  $T = 1.1, 1.5, 2.5, 3.5 T_c$  (from top to bottom). For comparison, we also show the analytically continued results (dashed curves) of the polynomial fit from [19] to  $n/T^3$  for imaginary chemical potential.

in slope observed for  $T = 1.1T_c$  at large  $\mu_i/T_c$ , its coefficients  $a$  and  $b$  are temperature and quark mass dependent. In contrast, the QPM parameters  $\lambda$  and  $T_s$  are once adjusted to  $n/T^3$  at  $T = 1.1T_c$  (cf. Fig. 1) and then kept fixed for all temperatures and chemical potentials. In addition, the behavior of analytic continuations of polynomial fits decisively depends on the considered order in  $\mu_i^2$  (cf. discussion in [9,27]). The QPM, in contrast, contains all orders of  $\mu_i^2$  respecting the symmetry  $\ln Z(\mu) = \ln Z(-\mu)$ . As evident from Fig. 2, we point out that close to  $\mu_c(T)$  a sensible analytic continuation is needed.

In Fig. 3, the net baryon density  $n_B/T^3$  is exhibited as a function of  $T/T_c$  for constant imaginary (solid curves) as well as for real baryochemical potential  $\mu_B = 3\mu$  (dashed curves). As for small baryochemical potentials or large temperatures  $n_B$  depends linearly on  $\mu$  [cf. Eq. (2)]; the results for real  $\mu_B$  significantly deviate from the original results for imaginary chemical potential only at large  $\mu_B$  and temperatures close to  $T_c$ . Note that in these considerations  $\mu_B$  is restricted to  $|\mu_B| \leq \pi T$ .

Susceptibilities are quantities serving as measures of fluctuations. The quark number susceptibility  $\chi$  [cf. Eqs. (7) and (8)] is simply the derivative of the density in  $\mu_i$  direction. We exhibit  $\chi/T^2$  either at  $\mu = 0$  for various temperatures (Fig. 4, left panel) or for  $T = 1.1T_c$  for various values of  $\mu_i$  (Fig. 4, right panel). Clearly, if lattice QCD data for  $n(T, i\mu_i)$  are well described by a model, the model should also describe  $\chi(T, i\mu_i)$ . This is indeed the case, see Fig. 4, where both lattice QCD data as well as QPM results, are obtained by numerical differentiation of the net quark number density. The only concern that could arise is that derivatives enhance possible systematic differences between a model and the data. Figure 4 does not point to such a possibility.

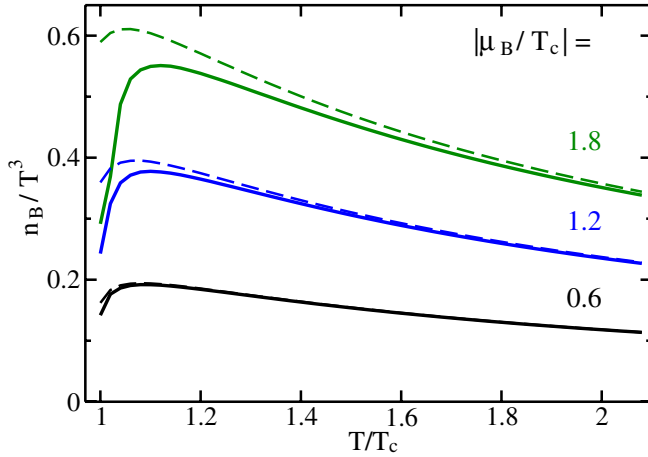


FIG. 3 (color online). Scaled net baryon density  $n_B/T^3$  as a function of  $T/T_c$  for constant imaginary  $\mu_B/T_c = 3i\mu_i/T_c$  (solid curves) and for corresponding real  $\mu_B/T_c$  (dashed curves). Note that for all temperatures,  $\partial n/\partial T > 0$  is fulfilled, as required from thermodynamic stability conditions.

### B. Deconfinement border line

The solution of Peshier's flow equation Eq. (5) is accomplished by the method of characteristics. As in [11], we consider the characteristic curve emerging at  $T = T_c$  and  $\mu = 0$  as an indicator of the pseudocritical line. This transition line has been calculated in lattice simulations [16] for imaginary chemical potential. The lattice QCD data have been analyzed by applying polynomial fits which were analytically continued to real  $\mu$  [16]. The results of such analytic continuations decisively depend on the chosen degree of the considered polynomial or ratios thereof, as discussed in [9,27].

In Fig. 5, the phase diagram is exhibited in specific coordinate systems. Negative values  $\mu_B^2 \leq 0$  indicate

purely imaginary baryochemical potential, whereas positive  $\mu_B^2 \geq 0$  indicate real  $\mu_B$ . Diamonds represent the polynomial fit [16] for both imaginary chemical potential and the corresponding analytically continued results. For comparison, we depict the QPM characteristic (solid) curve starting at  $T = T_c$  as solution of Peshier's flow equation Eq. (5) for imaginary chemical potential as well as for real  $\mu_B$ . The flatness of the curve in the exhibited  $\mu_B^2$  interval (left panel) signals the dominance of the  $\mu_B^2$  term in agreement with the polynomial fit findings in [16]. Note, however, that the QPM result contains all orders of  $\mu_B^2$ . We emphasize that our model parameters  $\lambda$  and  $T_s$  are adjusted to  $n(T, i\mu_i)$  at  $T = 1.1T_c$  and have proven above to describe at the same time  $n(T, i\mu_i)$  at  $T = 1.5, 2.5, 3.5T_c$ . In so far, the agreement of our characteristic curve emerging at  $T_c$  with the transition line in [16] is quite satisfying.

In Fig. 5 we also show the first two Roberge-Weiss transition lines (fat dashed curves characterized by [15]  $\mu_B^2/T_c^2 = -T^2/T_c^2 \pi^2(2k+1)^2$  for  $k = 1, 2$ ) at which thermodynamic quantities exhibit an analytic behavior at small temperatures, while the Roberge-Weiss transition represents a first-order phase transition (fat solid section) at sufficiently large  $T$ . In addition, the first  $Z_3$  center symmetry line is shown (dotted curve characterized by [15]  $\mu_B^2/T_c^2 = -T^2/T_c^2 \pi^2(2k)^2$  for  $k = 1$ ). The repeated copies of these sectors for  $k \geq 2$  are not displayed in Fig. 5; they reside in the left bottom edge.

Numerically, we find that the characteristic curve emerging at  $T = T_c$  and the first Roberge-Weiss transition line cross each other at  $T^E/T_c = 1.112$  and  $(\mu_B^E)^2/T_c^2 = -12.214$ , whereas the lattice QCD simulations [16,19] report  $T^E/T_c = 1.095$  and  $(\mu_B^E)^2/T_c^2 = -11.834$ . These tiny differences can hardly be resolved on the scale displayed in Fig. 5. For larger negative  $\mu_B^2$  the characteristic curve is mirrored at the Roberge-Weiss transition line (see

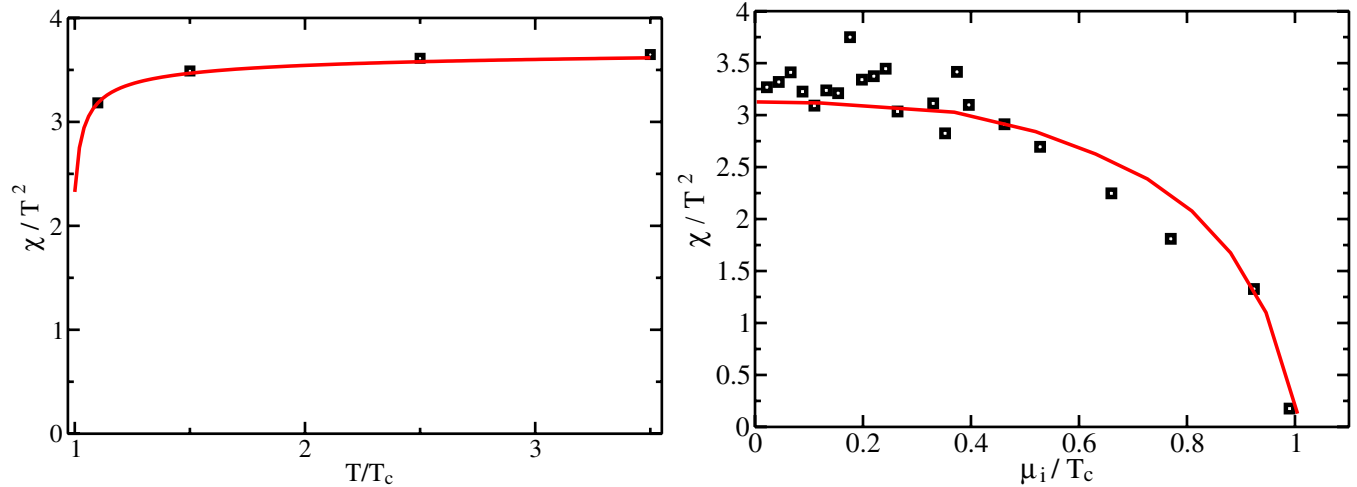


FIG. 4 (color online). Left: comparison of the QPM (solid curve) for the scaled quark number susceptibility  $\chi/T^2$  as a function of  $T/T_c$  for  $\mu = 0$  with the continuum estimate of the lattice QCD data in [19] (circles). Right: comparison of the QPM (solid curve) for  $\chi/T^2$  as a function of  $\mu_i/T_c \leq 1$  for  $T = 1.1T_c$  with the continuum estimate of the lattice QCD data in [21].

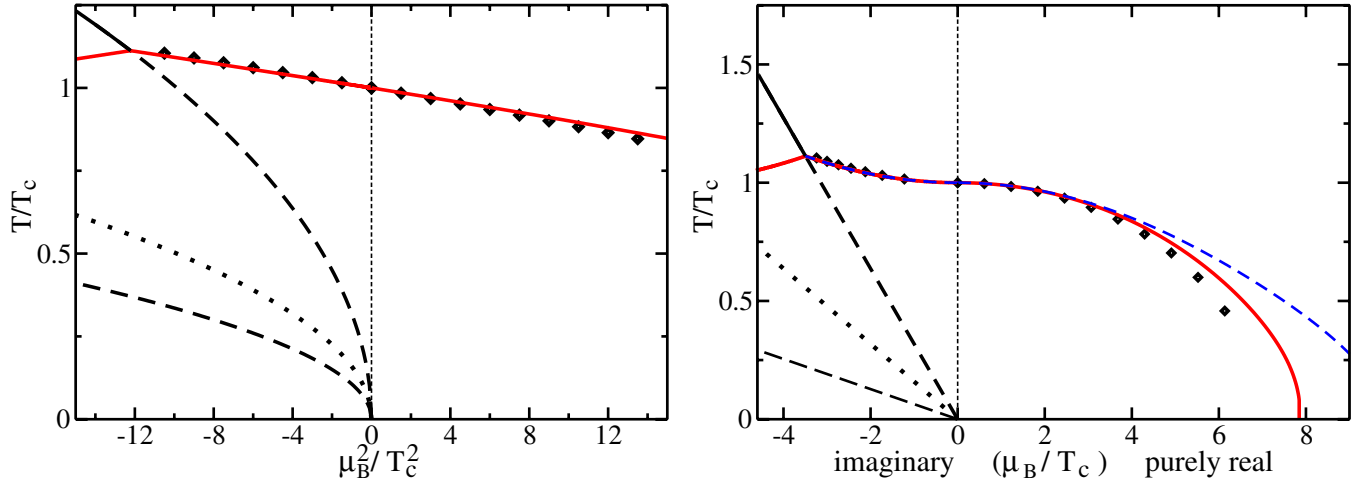


FIG. 5 (color online). Phase diagram for imaginary and real baryochemical potential. Left:  $T/T_c$  vs  $\mu_B^2/T_c^2$ . Right:  $T/T_c$  vs  $\mu_B/T_c$ . Details are explained in the text.

the section in the left top edge below the first Roberge-Weiss transition line in Fig. 5).

In the right panel of Fig. 5, we exhibit the phase diagram with the same notions as in the left panel, but with a linear abscissa  $\mu_B/T_c$ ; negative values of  $\mu_B/T_c$  are to be assigned to purely imaginary chemical potential, while positive values correspond to purely real values of  $\mu_B$ . As the coefficients in Peshier's flow equation Eq. (5) for real chemical potential obey  $a_T \rightarrow 0$  for  $\mu \rightarrow 0$  and  $a_\mu \rightarrow 0$  for  $T \rightarrow 0$ , the characteristic curves, including the one crossing the  $T$  axis at  $T_c$ , approach the  $T = 0$  and  $\mu_B = 0$  axes perpendicularly. Deviations between QPM results for real  $\mu_B$  and the polynomial fit become visible for  $\mu_B \geq 330$  MeV. In addition, we exhibit the solution of Peshier's flow equation starting at  $T_c$  for a different set of QPM parameters (cf. Sec. IVA) by the dashed line. For imaginary chemical potential, both results are indistinguishable, whereas for real  $\mu$  deviations become visible for  $\mu_B/T_c \geq 2$  signaling again that small deviations in the imaginary chemical potential sector result in larger deviations in the sector of real  $\mu$ . This makes predictions about the onset of possible deconfinement effects at small  $T$  and real  $\mu$  difficult.

### C. Quark mass dependence

In this subsection, we study the influence of a different approximation of the quark dispersion relation on the QPM results. In particular, we concentrate on the characteristic curve emerging at  $T = T_c$ . Apart from Eq. (3), another conceivable approximation of the quark dispersion relation is given by

$$\omega_q^2 = k^2 + m_q^2 + 2m_q M_+ + 2M_+^2 \quad (9)$$

as for instance employed and successfully compared with lattice QCD data in [11,28] with  $M_+^2$  from Eq. (4). This approximation of  $\omega_q$  is motivated from perturbative con-

siderations of the high temperature limit of the renormalized quark propagator for small quark masses  $m_q$  [29] and the assumption that the relation between asymptotic mass and plasma frequency known for  $m_q = 0$  is approximately true also for small  $m_q$  [30]. Changing the approximation of the dispersion relation  $\omega_q$  demands a readjustment of the parameters in the effective coupling  $G^2(T, \mu = 0)$  in Eq. (6) in order to appropriately describe the lattice QCD data of  $n/T^3$  and causes changes in Peshier's flow equation (see Appendix A). The QPM parameters for using Eq. (9) adjusted to the continuum estimate of the  $n/T^3$  data at  $T = 1.1T_c$  read  $T_s = 0.976T_c$  and  $\lambda = 95$  implying that the divergence in  $G^2(T, \mu = 0)$  is located at  $T = 0.987T_c$ . With this new parametrization, the agreement between QPM and continuum extrapolated lattice QCD data is nearly as perfect as observed in Fig. 1 (at most 3% deviations). However, it indicates that Eq. (3) might be somewhat more suitable than Eq. (9) as quark dispersion relation. The influence on the characteristic curve emerging at  $T = T_c$  when employing Eq. (9) instead of Eq. (3) is negligible for imaginary chemical potential. For real  $\mu_B/T_c$ , the difference between both parametrizations is also very tiny and approximately 1.5% at small temperatures.

In addition, we can discuss the quark mass dependence of the found results by performing a naive chiral extrapolation  $m_q \rightarrow 0$ . For imaginary chemical potential, quark mass effects turn out to be negligible independent of the specific quark dispersion relation used. For real  $\mu_B/T_c$ , quark mass effects are also small and visible only for very small temperatures. The differences between using  $m_q = 0.2T$  and  $m_q = 0$  are less than 1% when employing Eq. (3) and at most 3% when employing Eq. (9). In both cases, decreasing quark masses imply a larger curvature of the characteristic curves and thus a smaller critical chemical potential at  $T = 0$ . A similar minor quark mass depen-

dence with the same trend when decreasing  $m_q$  was found in lattice QCD simulations [31].

Another sensitive measure for the quark mass dependence of the net baryon density  $n_B$  is the chemical potential dependence of the chiral condensate  $\langle\bar{\psi}\psi\rangle$  which are related to each other by a Maxwell relation [19,21]. Within the QPM, the  $\mu$  dependence of  $\langle\bar{\psi}\psi\rangle$  is fairly well described and will be reported elsewhere. We note that simply putting  $m_q = 0$  but keeping the parametrization of  $G^2(T, \mu = 0)$  fixed modifies  $n/T^3$  by less than 1% for the considered range of temperatures and chemical potentials. In principle, however, a general quark mass dependence of the parameters  $T_s$  and  $\lambda$  in the effective coupling would be conceivable. Because of the minor effects observed, we restrict our further considerations to quark dispersion relation Eq. (3) in the following.

#### D. $\mu$ dependence of the quasiparticle masses

In [18], the lattice QCD data [32] have been discussed with the goal to extract the relevant excitation modes from thermodynamic bulk quantities. The explicit  $\mu$  dependence of the quasiparticle masses has been named BKS effect. In order to test the importance of the BKS effect on the found results, we omitted the  $\mu_i^2/\pi^2$  terms in the quasiparticle dispersion relations or flipped their signs though leaving the dependence of  $G^2$  on  $\mu_i$  (Peshier's flow equation) unchanged. While changing in this way the quasiparticle masses, we keep the QPM parameters from Sec. III A fixed. In fact, neglecting simply the term  $\propto \mu_i^2/\pi^2$  in Eq. (4) [or Eq. (A4) below],  $n/T^3$  is only affected for large  $\mu_i$ , where the attenuation of  $\mu_i^2$  by  $1/\pi^2$  becomes smaller and the term proportional to  $\mu_i^2$  cannot be neglected compared to the term proportional to  $T^2$ . This implies that for larger  $T$  significant effects can only be seen at sufficiently large values of  $\mu_i$ . Note, however, that  $\mu_i$  is restricted by  $\mu_i \leq \frac{\pi}{3}T$ . Similar effects can be observed when flipping the signs in the asymptotic mass expressions. Nonetheless, thermodynamic self-consistency of the QPM requires in both considered cases of changing the quasiparticle masses also changes in Peshier's flow equation (5) rendering the coefficients  $b$ ,  $a_T$  and  $a_{\mu_i}$  according to Maxwell's relation. In these thermodynamically self-consistent approaches, we find our results to be indistinguishable from the QPM results exhibited in Fig. 1 when employing the same parameters as in Sec. III A, i.e. found results seem to be rather independent of the explicit form of the  $\mu_i$  dependence in the asymptotic mass expressions. However, a general dependence of the asymptotic masses on the chemical potential seems to be important. When neglecting  $\mu_i$  completely in the quasiparticle dispersion relations, thermodynamic self-consistency dictates also an independence of  $T$  in  $M_\infty$  (and  $m_\infty$  in Appendix A) which significantly changes the results: even though the almost linear behavior of  $n/T^3$  for small  $\mu_i$  can be reproduced, the pronounced curvature for  $T = 1.1T_c$  at larger  $\mu_i$  cannot be

obtained under such an assumption. The  $\mu_i$  dependence of  $n/T^3$  is further discussed in Appendix A.

#### E. Scaling properties

In [24,33], a scaling of the ratio  $\Delta p/\Delta p^{SB}$  of the excess pressure in  $\mu_B$  direction was reported. Here, we find a similar scaling for the ratio  $n_B/n_B^{SB}$  as depicted in Fig. 6, where  $n_B^{SB}$  denotes the Stefan-Boltzmann expression of the net baryon density. When considering  $n_B/n_B^{SB}$  either for real or for imaginary chemical potential, in both cases,  $\mu_B$  effects become visible only in the vicinity of  $T_c$ . In fact, for the baryochemical potentials considered in Fig. 6, the ratio  $n_B/n_B^{SB}$  is found to be independent of  $\mu_B$  for  $T \geq 1.2T_c$ . Furthermore,  $n_B/n_B^{SB} = 1$  is approached only asymptotically, signaling the expected strong deviations from the free field behavior. Apart from the observed differences in the ratio between real and imaginary chemical potentials close to  $T_c$ , we find an interesting pattern:  $n_B/n_B^{SB}$  decreases with increasing baryochemical potential for real  $\mu_B$ , while the ratio increases in the case of imaginary chemical potential. This is partly caused by differences in  $n_B/T^3$  between real and imaginary chemical potential which become smaller for increasing temperature (cf. Figure 3). But it is also related to different signs in  $n_B^{SB}$  for real or imaginary chemical potential.

To be specific, in the case of real chemical potential,  $n_B$  can be expanded into a Taylor series in powers of  $\mu_B$  with expansion coefficients [32]  $c_k(T) = \frac{1}{k!} \frac{\partial^k (p(T, \mu)/T^4)}{\partial (\mu/T)^k} \Big|_{\mu=0}$ . The Stefan-Boltzmann expression for the net baryon density reads

$$n_B^{SB}(T, \mu_B) = \frac{N_f}{3} \frac{\mu_B}{3} T^2 + \frac{N_f}{3\pi^2} \left(\frac{\mu_B}{3}\right)^3. \quad (10)$$

Even though this expression for  $n_B^{SB}$  is correct only for a massless ideal gas, while  $n_B$  entering the ratio is evaluated for  $m_q = 0.2T$ , quark mass effects can safely be neglected (as discussed in Sec. III C). The ratio  $n_B/n_B^{SB}$  reads for small  $\mu_B/(3T)$

$$\frac{n_B}{n_B^{SB}} \approx \frac{2c_2}{N_f} + \frac{2}{N_f} \left(\frac{\mu_B}{3T}\right)^2 \left[2c_4 - \frac{c_2}{\pi^2}\right] + \mathcal{O}(\mu_B^4). \quad (11)$$

In the limit  $\mu_B \rightarrow 0$ , the ratio approaches  $2c_2/N_f = \frac{1}{4}\chi(T, \mu = 0)/T^2$  for  $N_f = 4$ . For small  $\mu_B/(3T)$ , i.e. for small  $\mu_B$  or large  $T$ ,  $\mu_B$  effects become small, thus explaining the observed scaling. Furthermore, as  $2c_4 - c_2/\pi^2 > 0$  for all temperatures  $T \geq T_c$  and remains approximately constant for  $T \geq 1.2T_c$  (cf. Sec. IV B), a fixed ratio  $n_B/n_B^{SB}$  requires increasing temperatures  $T$  for increasing  $\mu_B$ , explaining the observed ordering in Fig. 6. Close to  $T_c$ , deviations between exact results and the Taylor series expansion of  $n_B$  become larger with increasing  $\mu_B$ , such that the arguments presented here do not apply.

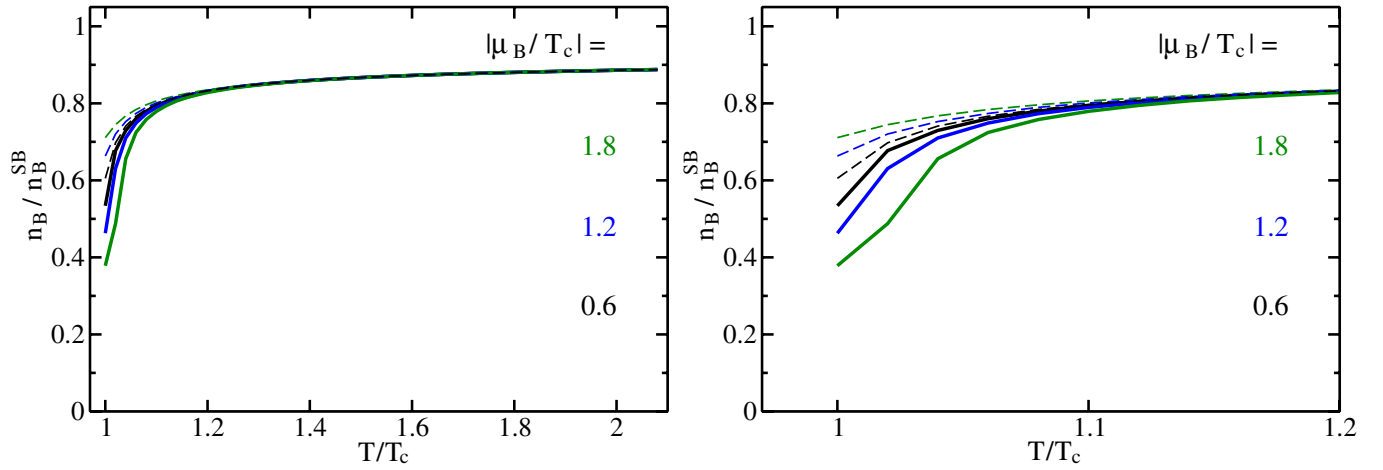


FIG. 6 (color online). Left: ratio  $n_B/n_B^{\text{SB}}$  as a function of  $T/T_c$  for different imaginary and real baryochemical potentials. Dashed curves represent results for imaginary baryochemical potential, with  $|\mu_B/T_c| = 0.6, 1.2, 1.8$  from bottom to top, while solid curves depict corresponding results for real  $\mu_B$ , with  $|\mu_B/T_c| = 0.6, 1.2, 1.8$  in inverted order, i.e. from top to bottom. Right: zoom into the region close to  $T_c$ .

In the case of imaginary chemical potential,  $n_B(T, i\mu_i)$  from Eq. (2) can be evaluated for small  $\mu_i$  by expanding the trigonometric functions in powers of  $\mu_i/T$  yielding also a Taylor series expansion similar to the one in the sector of real chemical potential. Within this approach, we find

$$n_B(T, i\mu_i) = i\left(\frac{2}{3}\tilde{c}_2\mu_i T^2 - \frac{4}{3}\tilde{c}_4\mu_i^3 + \dots\right), \quad (12)$$

where

$$\tilde{c}_k(T) = \frac{1}{k!i^k} \left. \frac{\partial^k (p(T, i\mu_i)/T^4)}{\partial (\mu_i/T)^k} \right|_{\mu_i=0} \equiv c_k(T). \quad (13)$$

Note that both  $\tilde{c}_k$  and  $c_k$  are real and  $\tilde{c}_k, c_k = 0$  for odd  $k$ . The Stefan-Boltzmann result for imaginary chemical potential reads

$$n_B^{\text{SB}}(T, i\mu_i) = i\left(\frac{N_f}{3}\mu_i T^2 - \frac{N_f}{3\pi^2}\mu_i^3\right) \quad (14)$$

and the ratio follows as  $\frac{n_B}{n_B^{\text{SB}}} \approx \frac{2\tilde{c}_2}{N_f} - \frac{2}{N_f}\left(\frac{\mu_B}{3T}\right)^2[2\tilde{c}_4 - \frac{\tilde{c}_2}{\pi^2}] + \mathcal{O}(\mu_B^4)$ . Similar to the considerations for real chemical potential, we observe a scaling with  $\mu_B/(3T)$  and in the limit  $\mu_B \rightarrow 0$ ,  $n_B/n_B^{\text{SB}} \rightarrow 2c_2/N_f = \frac{1}{4}\chi(T, \mu = 0)/T^2$  for  $N_f = 4$ . For imaginary chemical potential, however, the sign of the term proportional to  $\mu_B^2$  is flipped, explaining the different ordering observed in Fig. 6, i.e. at fixed  $T$ ,  $n_B/n_B^{\text{SB}}$  becomes larger with increasing  $\mu_B$ .

#### IV. COMPARISON WITH LATTICE QCD DATA AT $\mu = 0$

##### A. Pressure

Via the QPM, we have access to both real and imaginary chemical potentials. Thus, we can compare our results

based on the lattice QCD data of [19,21] with other lattice QCD calculations. In [34], a similar lattice set-up for calculating the pressure at  $\mu = 0$  for  $N_f = 4$  degenerate quark flavors with  $m_q = 0.2T$  on a lattice with  $N_\tau = 4$  and  $N_\sigma = 16$  was considered, though employing an improved lattice action. These lattice QCD data [34] require also a proper continuum extrapolation. We apply a similar strategy as in Sec. III A but now for the pressure, because its Stefan-Boltzmann limit is given in [34] for  $N_\tau = 4$ , and find  $d_{\text{lat}}^{(p)} = 0.839$  as continuum extrapolation factor. The difference between  $d_{\text{lat}}^{(p)}$  and  $d_{\text{lat}}^{(n)}$  in Sec. III is maybe a consequence of the different lattice actions used in the simulations [19,21,34] resulting in different cutoff effects on the data.

In Fig. 7, the continuum estimated lattice QCD data [34] (squares) for  $p/T^4$  as a function of  $T/T_c$  at  $\mu = 0$  are compared with the QPM (for details see Appendix A) using the parameters  $\lambda$  and  $T_s$  in  $G^2(T, \mu = 0)$  from Sec. III A adjusted to  $n/T^3$  at  $T = 1.1T_c$  for imaginary chemical potential. The integration constant  $B(T_c)$  adjusting the QPM value of  $p/T^4$  at  $\mu = 0$  and  $T = T_c$  to lattice QCD reads  $B(T_c) = 2.56T_c^4$  using again  $T_c = 163$  MeV. As evident from Fig. 7, the general trend of  $p/T^4$  and the behavior at large  $T$  is reproduced. Nevertheless,  $p/T^4$  shows deviations of up to 20% in the intermediate temperature region  $T \sim 1.5T_c$ . The same deviation pattern was already discussed in [14,24,28]. In fact, it seems to be a general feature, that fits to lattice QCD data in the sector of zero (nonzero) chemical potential underestimate (overestimate) the according results in the sector of nonzero (zero) chemical potential.

Considering, instead, an independent adjustment of the QPM parameters to  $p/T^4$  at  $\mu = 0$ , the comparison of the QPM with the continuum estimate of the lattice QCD data



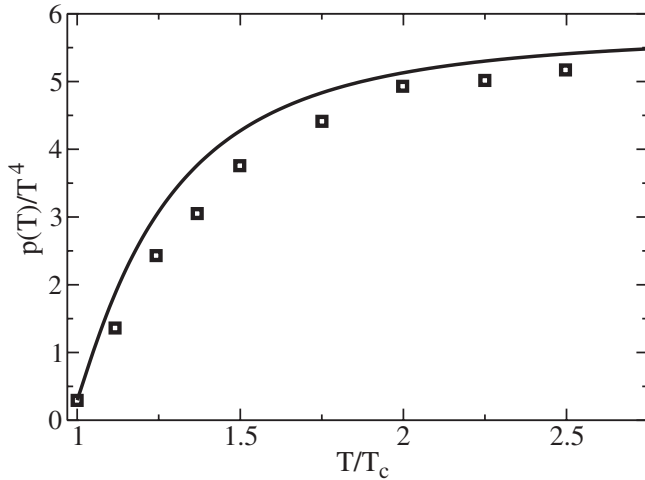


FIG. 7. Comparison of the QPM (solid curve, using parameters as in Sec. III A) for the scaled pressure  $p/T^4$  as a function of  $T/T_c$  at  $\mu = 0$  with the continuum estimate of the lattice QCD data [34] (squares).

is exhibited in Fig. 8 (left panel). We find an impressive agreement when adjusting  $T_s = 0.91T_c$ ,  $\lambda = 16$  and  $B(T_c) = 1.25T_c^4$  with  $T_c = 163$  MeV. With this new parametrization, we evaluate the net quark number density for imaginary chemical potential. The results (solid curves) are shown in the right panel of Fig. 8. At constant  $\mu_i/T_c$ , we find increasing deviations for decreasing temperatures, in particular close to the Roberge-Weiss transition, even though the change in slope close to  $\mu_c$  is qualitatively still reproduced. Furthermore, using this set of parameters results in the dashed curve in the right panel of Fig. 5 as characteristic curve emerging at  $T = T_c$  for real  $\mu_B$ . With respect to the observed deviations at  $T = 1.1T_c$  between

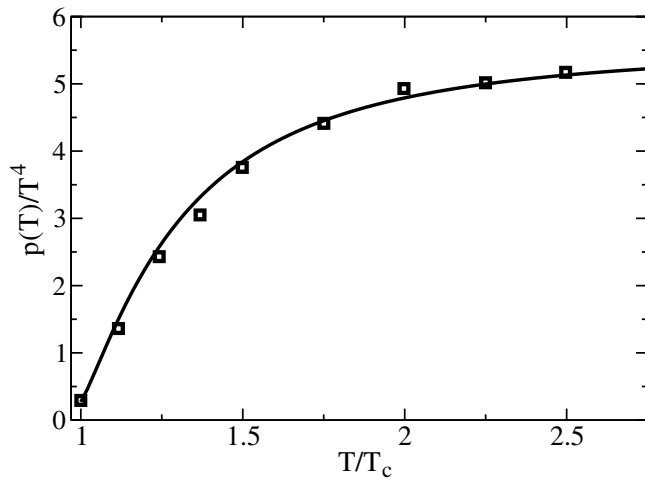


FIG. 8 (color online). Left: comparison of the QPM (solid curve) for  $p/T^4$  as a function of  $T/T_c$  at  $\mu = 0$  employing readjusted parameters (see text) with the continuum extrapolated lattice QCD data (squares) as exhibited in Fig. 7. Right: comparison of the QPM (solid curves, using the readjusted parameters) for  $n/T^3$  as a function of  $\mu_i/T_c$  for different  $T$  with the continuum extrapolated lattice QCD data (symbols) as exhibited in Fig. 1.

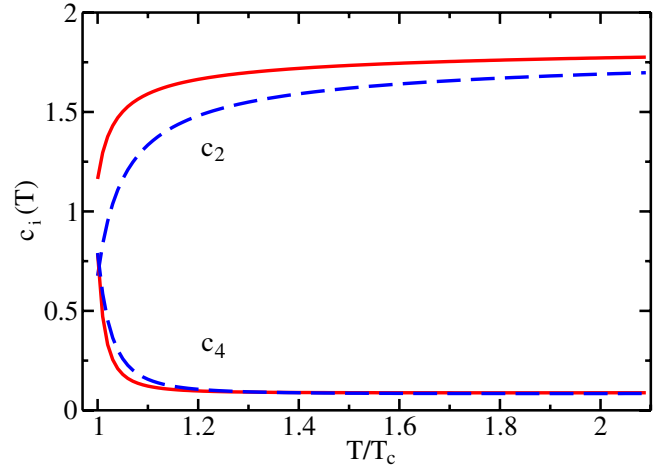
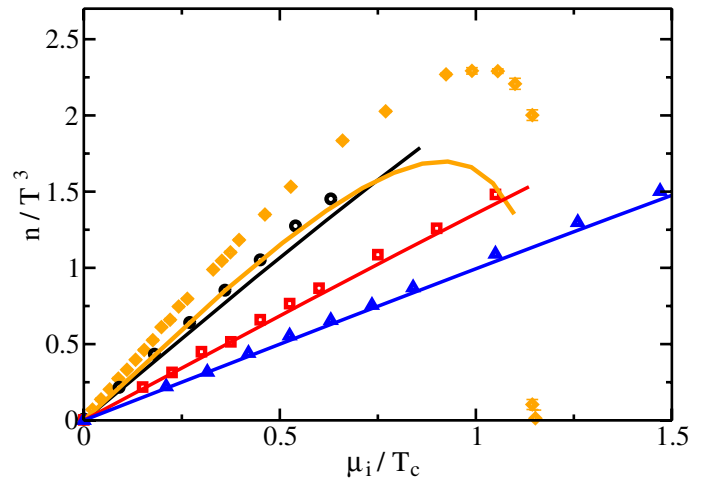


FIG. 9 (color online). Taylor series expansion coefficients  $c_2(T)$  (upper curves) and  $c_4(T)$  (lower curves) as function of  $T/T_c$  for  $N_f = 4$  employing the different parametrizations from Fig. 1 (solid curves) and Fig. 8 (dashed curves).

the lattice QCD data from [19,21] for  $n/T^3$  and the QPM with parameters adjusted to  $p/T^4$  (see right panel of Fig. 8), it is surprising that this characteristic curve agrees so well with the one considered in Sec. III B.

## B. Taylor expansion coefficients

Having the QPM parametrizations employed in Figs. 1 and 8 at hand, we can discuss their influence on the Taylor series expansion coefficients  $c_k(T)$  defined in Sec. III E for  $N_f = 4$  similar to studies for  $N_f = 2$  in [14]. In Fig. 9, we exhibit  $c_2(T)$  and  $c_4(T)$ :  $c_2(T) = \frac{1}{2}\chi(T, \mu = 0)/T^2$  shows some deviations between both parametrizations whereas  $c_4(T)$  agrees fairly well with visible deviations only in the



very vicinity of  $T_c$ . In addition, we observe that smaller  $c_0(T) \equiv p(T, \mu = 0)/T^4$  (cf. Fig. 7 and the left panel of Fig. 8) implies smaller  $c_2(T)$  as already pointed out in [28]. As mentioned in Sec. III A,  $n/T^3$  depicted as a function of  $\mu_i/T$  shows almost no temperature dependence for  $T \geq 1.5T_c$ . This is mainly due to the fact that  $c_2(T)$  (upper solid curve in Fig. 9) exhibits also a rather negligible temperature dependence for larger  $T$ . Furthermore,  $c_4(T)$  is sizeable only close to  $T_c$  and approaches its Stefan-Boltzmann limit  $1/\pi^2$  for  $T \geq 1.2T_c$ . Considering  $n_B/T^3$  in terms of a Taylor series expansion up to order  $\mathcal{O}(\mu^3)$ , the results for real and imaginary chemical potential differ only in the sign of the cubic term which is  $\propto c_4\mu^3$ . Thus, the net baryon density evaluated for real or imaginary chemical potential deviates only for larger chemical potentials and close to  $T_c$  as evident from Fig. 3.  $c_6(T)$  (not exhibited) deviates significantly from zero only for temperatures very close to  $T_c$  but can become of the same order of magnitude as  $c_4(T)$  at  $T = T_c$ .

Finally, we mention that the parametrization in Sec. IV A, optimized for reproducing the  $N_f = 4$  lattice QCD data of [34], can also be used to describe the Taylor coefficients  $c_{2,4}(T)$  from lattice QCD [32] for  $N_f = 2$  (although in these simulations a larger quark mass parameter  $m_q = 0.4T$  was used) as exhibited in the left panel of Fig. 10 (dashed curves). In doing so, we keep  $\lambda$  and  $T_s$  adjusted to  $N_f = 4$  lattice QCD data fixed and change merely from  $N_f = 4$  to  $N_f = 2$  in the thermodynamic expressions of the QPM. In fact, we find deviations of about 10% close to  $T_c$  and less than 5% for  $T \geq 1.2T_c$  between QPM and [32] for  $c_2(T)$ . While this coincidence might be accidental, one could also argue that the quasiparticle model catches correctly the flavor dependence. In contrast, employing the parametrization from Sec. III A

gives a pattern resembling Fig. 9. Even though deviations between both parametrizations are obvious, the ratio  $c_4/c_2$  is rather insensitive with respect to the employed parametrization for  $T \geq 1.2T_c$  approaching  $1/(2\pi^2)$  as shown in the right panel of Fig. 10.

## V. SUMMARY AND DISCUSSION

In summary we extend our effective quasiparticle model and compare it with lattice QCD data for purely imaginary chemical potential. Despite the fact that our phenomenological model does not exhibit the Roberge-Weiss periodicity of full QCD, it is able to describe the available lattice QCD data [16,19,21] impressively well. In particular, the drastic change in slope of  $n/T^3$  close to the critical chemical potential  $\mu_c/T = \pi/3$  of the Roberge-Weiss transition can be described. This is entirely due to the BKS effect [18], i.e. a consequence of chemical potential dependent quasiparticle masses. A thermodynamically consistent investigation of the importance of the  $\mu_i$  dependence in the quasiparticles' asymptotic masses shows that the found results are independent of the chosen explicit form of the  $\mu_i$  dependence. Nonetheless, the pronounced structures cannot be reproduced when the quasiparticle masses would be completely independent of  $\mu_i$ . In this respect, the  $\mu_i$  dependence implemented in the model is confirmed. Another evidence is the comparison of the QPM result for the characteristic curve emerging at  $T = T_c$  with the phase transition line evaluated in lattice QCD simulations [16]. For the Roberge-Weiss transition, we find critical values of temperature and baryochemical potential close to the ones given in [16]. The successful comparison points to the correctness of Peshier's flow equation as a tool for transporting information from  $\mu = 0$  to nonzero  $\mu$  which is of particular importance for the knowledge of the equa-

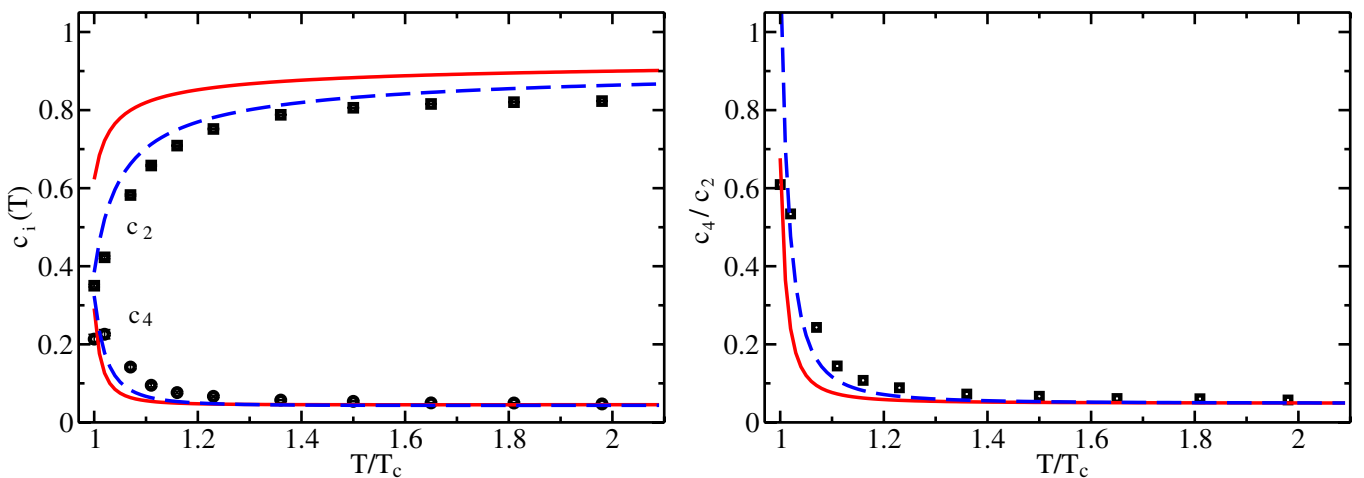


FIG. 10 (color online). Left: comparison of lattice QCD data [32] for  $N_f = 2$  for  $c_2(T)$  (squares) and  $c_4(T)$  (circles) as a function of  $T/T_c$  with the QPM for  $N_f = 2$ . Solid curves represent results applying QPM parameters as in Fig. 1 adjusted to  $n/T^3$  while dashed curves represent results applying the parametrization of Fig. 8 adjusted to  $p/T^4$  at  $\mu = 0$ . Right: ratio  $c_4/c_2$  as a function of  $T/T_c$  for both parametrizations.

tion of state at larger baryon densities relevant for CERN-SPS and upcoming FAIR.

With the found QPM parametrization describing lattice QCD data in the sector of purely imaginary chemical potential at hand, we can also compare with an independent set of lattice QCD data [34] obtained at  $\mu = 0$ . We find some deviations for the pressure in the intermediate temperature region which might account for the different lattice actions used in the calculations but could also signal to some extent a disagreement of results obtained at  $\mu = 0$  and nonzero  $\mu$ , as already discussed in [14,28]. In this context we emphasize that the comparison of thermodynamic models with lattice QCD data is hampered by the lacking systematic continuum extrapolation of the latter.

*Ab initio* it is not clear whether the assumed quasiparticle excitations represent the proper description of QCD thermodynamics also in the region close to  $T_c$ . The success of the present comparison lends some credibility into the picture of quasiquark excitations with a mass gap. This is in line with findings in [35], where also a striking deviation from the perturbative excitation pattern close to  $T_c$  has been found. Nevertheless, it would be premature to claim that the strongly coupled hot quark-gluon medium is entirely described by the presently used quasiparticles. For instance, excitation modes like plasminos and longitudinal gluons are not included in the model. Furthermore, finite width effects of the quasiparticles and Landau damping are neglected. One should keep in mind that thermodynamic bulk properties are sensitive essentially to excitations with hard momenta, i.e.  $k \sim T, \mu$ . There may be a variety of soft and ultrahard excitations rendering the picture of the strongly coupled quark-gluon plasma into a much more involved scenario, in line with the complexity of QCD.

Our model is far from being an *ab initio* calculation as attempted in [36]. But, in particular, the flexibility of the introduced effective coupling  $G^2$  allows for curing possible deficits in the dynamical degrees of freedom. Apart from that, the model is highly nonperturbative as it can be formulated in terms of an infinite series in powers of the coupling, though, making contact with perturbation theory, as the first terms coincide with perturbative QCD and asymptotically  $G^2$  approaches the running QCD coupling.

Finally, we remind the reader that we consider here a fairly special case of four degenerate quark flavors. Despite of the known sensitivity of particular features of QCD on the flavor content, some scaling properties of thermodynamic bulk properties may be useful for an orientation in thermodynamic state space.

## ACKNOWLEDGMENTS

The authors gratefully acknowledge stimulating and enlightening discussions with M. P. Lombardo, whom we also thank for supplying lattice QCD data in an early stage of these investigations. Furthermore, we thank P. de

Forcrand for interesting conversations. The work is supported by BMBF 06DR136, GSI-FE, and EU-I3HP.

## APPENDIX A: FLOW EQUATION FOR IMAGINARY CHEMICAL POTENTIAL

The QPM pressure for imaginary chemical potential reads

$$p(T, i\mu_i) = \sum_{a=q,g} p_a(T, i\mu_i) - B(T, i\mu_i) \quad (\text{A1})$$

with partial pressures

$$p_q(T, i\mu_i) = \frac{d_q}{2\pi^2} T \int_0^\infty dk k^2 (\ln[1 + e^{(i\mu_i - \omega_q)/T}] + \ln[1 + e^{(-i\mu_i - \omega_q)/T}]), \quad (\text{A2})$$

$$p_g(T, i\mu_i) = -\frac{d_g}{\pi^2} T \int_0^\infty dk k^2 \ln[1 - e^{-\omega_g/T}] \quad (\text{A3})$$

for quarks and gluons, respectively, where  $d_q = 2N_c N_f$  and  $d_g = N_c^2 - 1$ . The quasiparticle dispersion relations read  $\omega_q^2 = k^2 + m_q^2 + 2M_+^2 \equiv k^2 + M_\infty^2$  with  $M_+^2$  given in Eq. (4) and  $\omega_g^2 = k^2 + m_\infty^2$  with asymptotic mass

$$m_\infty^2 = \frac{1}{12} \left( [2N_c + N_f] T^2 - \frac{3}{\pi^2} N_f \mu_i^2 \right) G^2(T, i\mu_i). \quad (\text{A4})$$

Assuming that all  $T$  and  $\mu_i$  dependence of the function  $B$  is encoded in the asymptotic mass expressions  $M_\infty$  and  $m_\infty$ , thermodynamic consistency is fulfilled from the stationarity conditions  $\partial p / \partial M_\infty^2 = \partial B / \partial M_\infty^2$  and  $\partial p / \partial m_\infty^2 = \partial B / \partial m_\infty^2$  [37] such that entropy density  $s$  and net quark number density  $n$  are obtained from standard thermodynamic relations. The purely real result for  $s = s_q + s_g$  reads

$$s_q(T, i\mu_i) = \frac{d_q}{2\pi^2 T} \int_0^\infty dk k^2 \left\{ \frac{(\frac{4}{3}k^2 + M_\infty^2)}{\omega_q} [f_q^+ + f_q^-] - i\mu_i [f_q^+ - f_q^-] \right\}, \quad (\text{A5})$$

$$s_g(T, i\mu_i) = \frac{d_g}{\pi^2 T} \int_0^\infty dk k^2 \frac{(\frac{4}{3}k^2 + m_\infty^2)}{\omega_g} \frac{1}{(e^{\omega_g/T} - 1)}, \quad (\text{A6})$$

where  $f_q^\pm = (e^{(\omega_q \mp i\mu_i)/T} + 1)^{-1}$  and  $n$  is given in Eq. (1). Then, the function  $B$  is determined as appropriate line integral with integration constant  $B(T_c)$ . The quasilinear partial differential equation Eq. (5) to be solved for  $G^2(T, i\mu_i)$  follows from Maxwell's relation

$$\frac{\partial s}{\partial(i\mu_i)} = \frac{\partial^2 p}{\partial(i\mu_i)\partial T} = \frac{\partial^2 p}{\partial T \partial(i\mu_i)} = \frac{\partial n}{\partial T}, \quad (\text{A7})$$

where the explicit derivative terms cancel each other leaving

$$\frac{\partial n}{\partial M_\infty^2} \frac{\partial M_\infty^2}{\partial T} = \frac{\partial s_q}{\partial M_\infty^2} \frac{\partial M_\infty^2}{\partial(i\mu_i)} + \frac{\partial s_g}{\partial m_\infty^2} \frac{\partial m_\infty^2}{\partial(i\mu_i)}. \quad (\text{A8})$$

Omitting the overall factor of  $i$  in  $\partial n/\partial M_\infty^2$ ,  $\partial M_\infty^2/\partial(i\mu_i)$ , and  $\partial m_\infty^2/\partial(i\mu_i)$ , the coefficients of Eq. (5) read

$$b = \left(\frac{C_f}{2} T G^2 + 2m_q a\right) I_1 - \frac{3}{6\pi^2} N_f \mu_i G^2 I_2 - \frac{C_f}{2\pi^2} \mu_i G^2 I_3, \quad (\text{A9})$$

$$a_T = -\frac{C_f}{4} \left(T^2 - \frac{\mu_i^2}{\pi^2}\right) I_1, \quad (\text{A10})$$

$$a_{\mu_i} = -\frac{1}{12} \left([2N_c + N_f] T^2 - \frac{3}{\pi^2} N_f \mu_i^2\right) I_2 - \frac{C_f}{4} \left(T^2 - \frac{\mu_i^2}{\pi^2}\right) I_3, \quad (\text{A11})$$

where  $C_f = (N_c^2 - 1)/(2N_c)$  and the integral expressions explicitly read

$$I_1 = \frac{d_q}{2\pi^2 T} \int_0^\infty dk \frac{k^2}{\omega_q} \times \frac{(e^{\omega_q/T} \sin(\mu_i/T) - e^{3\omega_q/T} \sin(\mu_i/T))}{(e^{2\omega_q/T} + 2e^{\omega_q/T} \cos(\mu_i/T) + 1)^2}, \quad (\text{A12})$$

$$I_2 = \frac{d_g}{\pi^2 T} \int_0^\infty dk \frac{k^2}{\omega_g} \frac{1}{(e^{\omega_g/T} - 1)} \left(1 - \frac{(\frac{4}{3}k^2 + m_\infty^2)}{2\omega_g^2} \left[1 + \frac{\omega_g}{T} \frac{e^{\omega_g/T}}{(e^{\omega_g/T} - 1)}\right]\right),$$

$$I_3 = \frac{d_q}{2\pi^2 T} \int_0^\infty dk \frac{k^2}{\omega_q} \left(\frac{2e^{\omega_q/T} \cos(\mu_i/T) + 2}{e^{2\omega_q/T} + 2e^{\omega_q/T} \cos(\mu_i/T) + 1} \left[1 - \frac{(\frac{4}{3}k^2 + M_\infty^2)}{2\omega_q^2}\right] - \frac{(\frac{4}{3}k^2 + M_\infty^2)}{2\omega_q T}\right) \times \frac{(2e^{3\omega_q/T} \cos(\mu_i/T) + 4e^{2\omega_q/T} + 2e^{\omega_q/T} \cos(\mu_i/T))}{(e^{2\omega_q/T} + 2e^{\omega_q/T} \cos(\mu_i/T) + 1)^2} + \frac{\mu_i (e^{\omega_q/T} \sin(\mu_i/T) - e^{3\omega_q/T} \sin(\mu_i/T))}{T (e^{2\omega_q/T} + 2e^{\omega_q/T} \cos(\mu_i/T) + 1)^2}. \quad (\text{A13})$$

The term in  $b$  proportional to  $a$  stems from assuming temperature dependent quark masses  $m_q = aT$  as employed in some lattice QCD performances, e.g. [19,21,32,34,38].

The quark number susceptibility  $\chi$  in Eq. (7) is found to be symmetric when replacing  $\mu_i$  by  $-\mu_i$  because the same holds true for  $\partial G^2/\partial \mu_i$ . From Eq. (5) we find

$$\frac{\partial G^2}{\partial \mu_i} = \frac{b}{a_{\mu_i}} - \frac{a_T}{a_{\mu_i}} \frac{\partial G^2}{\partial T}. \quad (\text{A14})$$

For the individual expressions entering Eq. (A14) we find  $I_1 \rightarrow -I_1$ ,  $I_2 \rightarrow I_2$  and  $I_3 \rightarrow I_3$  for  $\mu_i \rightarrow -\mu_i$  such that  $b \rightarrow -b$ ,  $a_T \rightarrow -a_T$  and  $a_{\mu_i} \rightarrow a_{\mu_i}$ . In addition, a Taylor series expansion of  $G^2(T, i\mu_i)$  in powers of  $\mu_i$  consists only of even powers in  $\mu_i$  [13,14] such that  $\partial G^2/\partial T$  is symmetric under  $\mu_i \rightarrow -\mu_i$ . In the limit  $\mu_i \rightarrow 0$ , we find  $\partial G^2/\partial \mu_i \rightarrow 0$  as  $b \rightarrow 0$ ,  $a_T \rightarrow 0$  but  $a_{\mu_i}$  and  $\partial G^2/\partial T$  remain nonzero.

When employing the quark dispersion relation Eq. (9), the coefficients of the flow equation render to

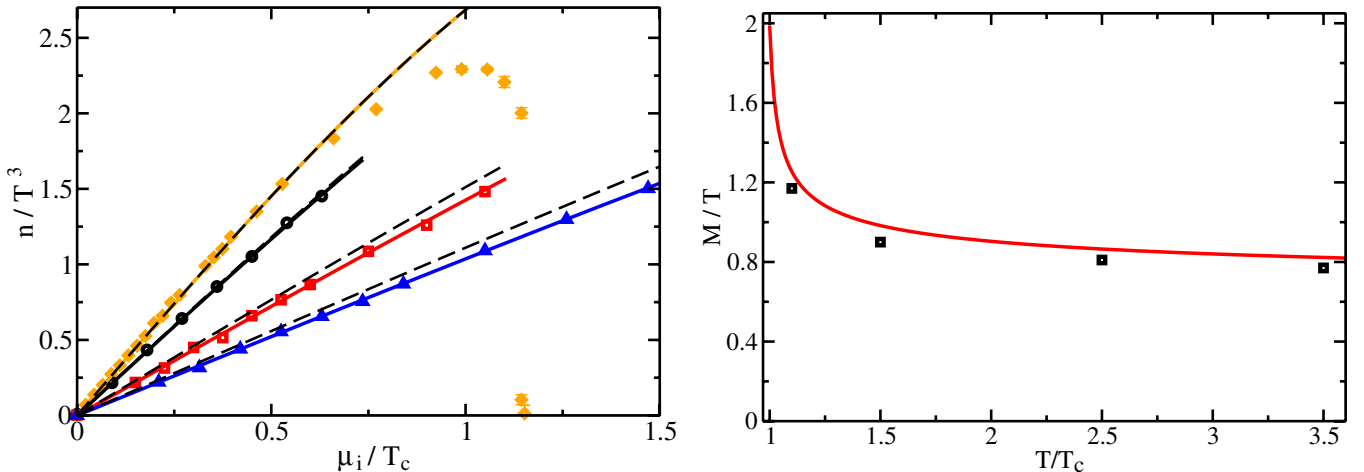


FIG. 11 (color online). Left: comparison of ideal gas results for  $n/T^3$  as a function of  $\mu_i/T_c$  employing either a constant mass parameter  $M = 0.21$  GeV (dashed curves) or readjusting  $M/T = 1.17, 0.90, 0.81, 0.77$  for  $T = 1.1, 1.5, 2.5, 3.5 T_c$  (solid curves from top to bottom) with the continuum extrapolated lattice QCD data (symbols) as exhibited in Fig. 1. Right: comparison of found  $M/T$  (squares) as a function of  $T/T_c$  with the asymptotic quark mass  $M_\infty/T$  of the QPM at  $\mu = 0$  employing  $T_s = 0.96 T_c$  and  $\lambda = 56$  as in Sec. III A.

$$b = \left[ \left( \frac{C_f}{4} + m_q \sqrt{\frac{C_f}{8(T^2 - \frac{\mu_i^2}{\pi^2})G^2}} \right) 2TG^2 + 2m_q a + 2aM_+ \right] I_1 - \frac{3}{6\pi^2} N_f \mu_i G^2 I_2 - 2 \frac{\mu_i}{\pi^2} G^2 \left( \frac{C_f}{4} + m_q \sqrt{\frac{C_f}{8(T^2 - \frac{\mu_i^2}{\pi^2})G^2}} \right) I_3, \quad (\text{A15})$$

$$a_T = - \left( T^2 - \frac{\mu_i^2}{\pi^2} \right) \left( \frac{C_f}{4} + m_q \sqrt{\frac{C_f}{8(T^2 - \frac{\mu_i^2}{\pi^2})G^2}} \right) I_1, \quad (\text{A16})$$

$$a_{\mu_i} = - \frac{1}{12} \left( [2N_c + N_f] T^2 - \frac{3}{\pi^2} N_f \mu_i^2 \right) I_2 - \left( T^2 - \frac{\mu_i^2}{\pi^2} \right) \left( \frac{C_f}{4} + m_q \sqrt{\frac{C_f}{8(T^2 - \frac{\mu_i^2}{\pi^2})G^2}} \right) I_3. \quad (\text{A17})$$

### APPENDIX B: PARAMETRIZING THE $\mu_i$ DEPENDENCE

In Sec. III, we found a general dependence of the quasiparticle dispersion relations on temperature and chemical potential to be of utmost importance for the successful description of lattice QCD data. This shall be illustrated in some more detail by considering the net quark number density in Eq. (1) of an ideal gas with dispersion relation  $\omega_q^2 = k^2 + M^2$ . In principle, thermodynamic self-consistency demands either a dependence of  $M$  on both  $T$  and  $\mu_i$ , or neither a  $T$  nor a  $\mu_i$  dependence of  $M$ . In the latter case of constant  $M$ , we adjust  $M = 0.21$  GeV in order to describe the continuum extrapolated lattice QCD data of  $n/T^3$  (cf. Fig. 1) at  $T = 1.1T_c$  for small  $\mu_i/T_c$ . The corresponding QPM results for  $T = 1.1, 1.5, 2.5, 3.5T_c$  are then exhibited in the left panel of Fig. 11 (dashed curves). At  $T = 1.1T_c$ , we find increasing deviations from the lattice QCD data for  $\mu_i/T_c > 0.66$ , in particular, in the vicinity of the Roberge-Weiss critical chemical potential  $\mu_c(T)$ , where the pronounced curvature cannot be reproduced. This was already discussed in [21] by considering the ratio  $n(\mu_i)/n(\mu_i)_{\text{free}}$  signaling clear deviations of the

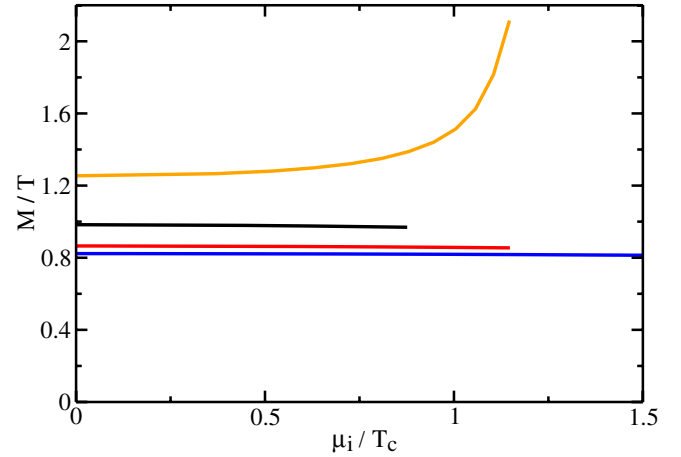


FIG. 12 (color online). Asymptotic quark mass  $M_\infty/T$  of the QPM (solid curves) as a function of  $\mu_i/T_c$  for  $T = 1.1, 1.5, 2.5, 3.5T_c$  (from top to bottom) employing the QPM parameters from Sec. III A.

lattice QCD data from a free (ideal) gas behavior. Furthermore, by increasing  $T$  but keeping  $M$  fixed, the description of the lattice QCD data becomes less and less accurate for smaller  $\mu_i/T_c$  suggesting a general dependence of  $M$  on  $T$ . Readjusting  $M$  individually for each temperature, ignoring for the moment being thermodynamic self-consistency, the results are depicted by solid curves in the left panel of Fig. 11. The found scaled mass parameters  $M/T$  for the temperatures considered here are exhibited in the right panel of Fig. 11 (squares) and compared with the scaled asymptotic quark mass  $M_\infty/T$  of the QPM at  $\mu = 0$  (solid curve) employing the parametrization of Sec. III A. Both results agree fairly well, indicating that nonzero chemical potential effects are tiny for small  $\mu_i/T$  but become sizeable close to  $\mu_c(T)$  as also visualized in Fig. 12. In Fig. 12, the scaled asymptotic quark mass  $M_\infty/T$  of the QPM is exhibited as a function of  $\mu_i/T_c$  for constant  $T$  using the QPM parametrization of Sec. III A perfectly describing  $n/T^3$  in Fig. 1. For increasing  $T$ ,  $M_\infty/T$  shows decreasing sensitivity on  $\mu_i$  while nonzero chemical potential effects become important close to  $\mu_c = \frac{\pi}{3}T$ .

- [1] F. Karsch, Lect. Notes Phys. **583**, 209 (2002).
- [2] T. Hatsuda, Workshop on the Physics of High Baryon Density, 2005, GSI, Darmstadt, Germany (unpublished); T. Hatsuda and T. Kunihiro, Phys. Rev. Lett. **55**, 158 (1985).
- [3] Proceedings of Critical Point and Onset of Deconfinement—3rd International Workshop, 2006, Florence, Italy, edited by F. Becattini (unpublished); 4th

- International Workshop, 2007, Darmstadt, Germany, edited by P. Senger *et al.* (unpublished).
- [4] M. Gyulassy and L. McLerran, Nucl. Phys. **A750**, 30 (2005).
- [5] D. A. Teaney, Phys. Rev. C **68**, 034913 (2003); J. Phys. G **30**, S1247 (2004); Nucl. Phys. **A785**, 44 (2007).
- [6] E. V. Shuryak and I. Zahed, Phys. Rev. D **70**, 054507 (2004); E. V. Shuryak, Nucl. Phys. **A750**, 64 (2005); A.

- Peshier and W. Cassing, Phys. Rev. Lett. **94**, 172301 (2005).
- [7] E. Laermann and O. Philipsen, Annu. Rev. Nucl. Part. Sci. **53**, 163 (2003).
- [8] O. Philipsen, Proc. Sci. LAT2005 (2006) 016; Proc. Sci. JHW2005 (2006) 012.
- [9] C. Schmidt, Proc. Sci. LAT2006 (2006) 021.
- [10] A. Peshier, B. Kämpfer, O. P. Pavlenko, and G. Soff, Phys. Lett. B **337**, 235 (1994); Phys. Rev. D **54**, 2399 (1996).
- [11] A. Peshier, B. Kämpfer, and G. Soff, Phys. Rev. C **61**, 045203 (2000); Phys. Rev. D **66**, 094003 (2002).
- [12] M. Bluhm, B. Kämpfer, R. Schulze, and D. Seipt, Eur. Phys. J. C **49**, 205 (2007).
- [13] M. Bluhm, Diploma Thesis, Technische Universität Dresden, 2004.
- [14] M. Bluhm, B. Kämpfer, and G. Soff, Phys. Lett. B **620**, 131 (2005).
- [15] A. Roberge and N. Weiss, Nucl. Phys. **B275**, 734 (1986).
- [16] M. D'Elia and M.-P. Lombardo, Phys. Rev. D **67**, 014505 (2003).
- [17] D. Seipt, Diploma Thesis, Technische Universität Dresden, 2007.
- [18] J. Liao and E. V. Shuryak, Phys. Rev. D **73**, 014509 (2006).
- [19] M. D'Elia and M.-P. Lombardo, Phys. Rev. D **70**, 074509 (2004).
- [20] M.-P. Lombardo, Prog. Theor. Phys. Suppl. **153**, 26 (2004); M. D'Elia, F. Di Renzo, and M.-P. Lombardo, in *International Workshop on Quantum Chromodynamics: Theory and Experiment*, edited by P. Colangelo *et al.*, AIP Conf. Proc. No. 806 (AIP, New York, 2006), p. 245.
- [21] M. D'Elia, F. Di Renzo, and M.-P. Lombardo, Phys. Rev. D **76**, 114509 (2007).
- [22] M.-P. Lombardo, Prog. Theor. Phys. Suppl. **153**, 26 (2004).
- [23] G. Boyd, J. Engels, F. Karsch, E. Laermann, C. Legeland, M. Lütgemeier, and B. Petersson, Nucl. Phys. **B469**, 419 (1996).
- [24] K. K. Szabo and A. I. Toth, J. High Energy Phys. 06 (2003) 008.
- [25] R. V. Gavai and S. Gupta, Phys. Rev. D **65**, 094515 (2002); Phys. Rev. D **67**, 034501 (2003); (private communication, March 2006).
- [26] R. V. Gavai and S. Gupta, Phys. Rev. D **68**, 034506 (2003).
- [27] M.-P. Lombardo, Proc. Sci., CPOD2006 (2006) 003.
- [28] M. Bluhm, B. Kämpfer, R. Schulze, D. Seipt, and U. Heinz, Phys. Rev. C **76**, 034901 (2007).
- [29] R. D. Pisarski, Nucl. Phys. **A498**, 423c (1989).
- [30] A. Peshier, arXiv:hep-ph/9809379.
- [31] C.R. Allton, S. Ejiri, S.J. Hands, O. Kaczmarek, F. Karsch, E. Laermann, C. Schmidt, and L. Scorzato, Phys. Rev. D **66**, 074507 (2002).
- [32] C.R. Allton, S. Ejiri, S.J. Hands, O. Kaczmarek, F. Karsch, E. Laermann, and C. Schmidt, Phys. Rev. D **68**, 014507 (2003); C.R. Allton, M. Döring, S. Ejiri, S.J. Hands, O. Kaczmarek, F. Karsch, E. Laermann, and K. Redlich, Phys. Rev. D **71**, 054508 (2005).
- [33] Z. Fodor, S.D. Katz, and K. K. Szabo, Phys. Lett. B **568**, 73 (2003); F. Csikor, G. I. Egri, Z. Fodor, S.D. Katz, K. K. Szabo, and A. I. Toth, Nucl. Phys. B, Proc. Suppl. **119**, 547 (2003).
- [34] J. Engels, R. Joswig, F. Karsch, E. Laermann, M. Lütgemeier, and B. Petersson, Phys. Lett. B **396**, 210 (1997).
- [35] F. Karsch and M. Kitazawa, Phys. Lett. B **658**, 45 (2007).
- [36] J.P. Blaizot, E. Iancu, and A. Rebhan, Phys. Rev. Lett. **83**, 2906 (1999); Phys. Lett. B **470**, 181 (1999); Phys. Rev. D **63**, 065003 (2001); Phys. Lett. B **523**, 143 (2001); Phys. Rev. D **68**, 025011 (2003); *Quark Gluon Plasma 3*, edited by R.C. Hwa and X.N. Wang (World Scientific, Singapore, 2004), p. 60.
- [37] M.I. Gorenstein and S.N. Yang, Phys. Rev. D **52**, 5206 (1995).
- [38] F. Karsch, E. Laermann, and A. Peikert, Phys. Lett. B **478**, 447 (2000).